Article

An acid-free process to prepare battery grade nickel and cobalt sulfates from complex resources

Qing Zhang [1,2,3], Xiaohong Zheng[2,3,4], Weiguang Lv[2,3], Mingming He[2], Wenyi Yan[2,3], Wenfang Gao[5], Pengge Ning[2,3], Hongbin Cao [1,2,3] ✉ & Zhi Sun [1,2,3] ✉

Nickel sulfate is a critical compound for lithium-ion batteries, mainly prepared from nickel sulfide concentrate (NSC). Typically, high-temperature smelting or high-pressure leaching is required to achieve high extraction rates for Ni and Co. Here, we demonstrate an acid-free atmospheric leaching process for effectively processing of NSC using a mechanochemical treatment. When a suitable intermediate phase of the NSC is obtained, the leaching efficiency for Ni and Co can reach 97.4% and 98.8%, respectively, while the main impure element, iron, almost remains in the solid phase. As a consequence, the leaching solution can be easily treated to prepare battery-grade $NiSO_4$. A technoeconomic analysis demonstrates that the acid-free process provides excellent economic advantages, with carbon emissions being reduced by 59.5%. This provides a sustainable alternative for processing complex sulfide resources and is expected to be applied to zinc and copper sulfide concentrates.

As the clean energy transformation of society promotes rapid deployment of the electric vehicle (EV) and battery storage industries[1,2], there is an urgent demand for critical metal resources such as battery-grade nickel (Ni) and cobalt (Co) sulfate. Considering the high dependence of the clean energy industry on metal resources such as Ni and Co, China, the United States, Canada, and Japan have listed them as critical minerals[3]. According to the United States Geological Survey (USGS)[4], land-based Ni-Co resources are mainly sulfide and laterite ores, with Ni sulfide deposits located mainly in Russia, Australia, Canada, southern Africa, and China[5]. Ninety percent of battery-grade Ni sulfate is reported to be produced from Ni sulfide concentrate (NSC), and over 90% of NSC is processed with pyrometallurgical process[6–8].

In a typical pyrometallurgical process, the NSC is smelted to form nickel matte, which is then subjected to oxygen pressure acid leaching to produce battery-grade Ni sulfate[9]. However, this process suffers from substaintial Ni and Co loss into the slag[10–12], and SO_2 emission into the off-gas[11,13], which place tremendous challenges on the economic and environmental sustainability of Ni and Co production[14,15]. To improve the yields of Ni and Co and reduce the environmental risks, hydrometallurgical processes including high-pressure ammoniacal leaching[16], high-pressure acid leaching[17,18], roasting-leaching[19,20], and bioleaching[21,22] processes, have been explored. Among them, high-pressure acid leaching (with sulfuric acid as the leaching agent and oxygen as the oxidant) has become the focus of industrial applications due to its fast leaching kinetic, lower chemical agent costs, and higher leaching efficiency[12]. The high-pressure acid leaching of NSC is mainly a sulfur oxidation process in which sulfur ion is oxidized to elemental sulfur or sulfuric acid, with Ni or Co being released from the solid into the solution. Nevertheless, at low

[1]School of Chemical Engineering, University of Chinese Academy of Sciences, Beijing 100190, China. [2]National Engineering Research Center of green recycling for strategic metal resources, Institute of Process Engineering, Chinese Academy of Sciences, Beijing 100190, China. [3]Chemistry and Chemical Engineering Data Center, Chinese Academy of Sciences, Beijing 100864, China. [4]School of Materials Science and Technology, China University of Geosciences (Beijing), Beijing 100083, China. [5]School of Energy and Environmental Engineering, Hebei University of Technology, Tianjin 30040l, China. ✉e-mail: hbcao@ipe.ac.cn; sunzhi@ipe.ac.cn

temperatures (<120 °C), the elemental sulfur (hard to oxidize[23,24]) generated during sulfur oxidation encapsulates unreacted NSC and hinders the oxidation, resulting in low Ni and Co leaching efficiencies[25,26]. To address this limitation, increased oxygen pressure and elevated temperature are typically required to achieve higher Ni and Co leaching efficiencies. However, these harsh operations raise costs and increase the proportion of elemental sulfur oxidation to sulfuric acid, thereby increasing the acidity of the leaching solution and inducing unwanted iron (Fe) leaching[27-32]. Thus, there is an urgent need to develop a leaching strategy that enables efficient leaching of Ni-bearing sulfides under mild conditions[33,34].
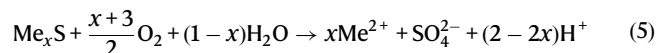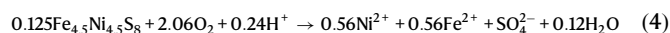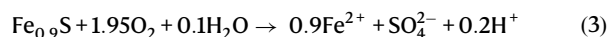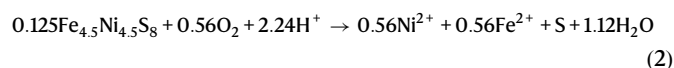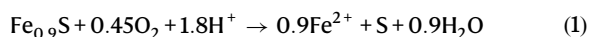
Mechanical activation enhances the reactivity of minerals by introducing mechanical energy, which enables efficient leaching of metals under mild conditions[35,36]. This eco-friendly method is considered as a promising process for extracting metals from refractory minerals[37,38] and solid waste[39,40]. During mechanical activation, the mechanical forces induced by mechanical energy could reduce particle size, break the symmetry of chemical bonds, and alter the crystalline structure's order, resulting in an increase in surface area, microstructural changes, and probable phase transformation[39,41]. These structural alterations are accompanied by an accumulation of system free energy, which significantly reduces the apparent reaction free energy for mineral decomposition, avoiding the use of harsh leaching conditions (e.g., high temperatures/pressures)[42]. However, until recently, the application of mechanical activation for the atmospheric leaching of sulfide minerals has relied on reagent-assisted milling or high-concentration acid leaching[43-45]. These processes not only elevated reagent consumption and undesirable metal dissolution but also posed environmental risks associated with high-salt wastewater. Inspired by the process in which sulfur-oxidizing bacteria utilize sulfide minerals to produce sulfuric acid in the atmospheric environment[46], it would be highly desirable if the metal leaching could be achieved by the atmospheric oxidation of NSC to produce sulfuric acid. The main challenge is identifying endogenous acid-generating sulfur species and properly breaking down the structure of NSC to generate active acid-producing sulfur species that can be oxidized in situ to produce acid to fulfill the acid consumption required for metal leaching.

In this work, undercoordinated sulfur was identified as an active acid-producing sulfur species, leading to the proposal of an acid-free and selective NSC atmospheric leaching process. At the end of leaching, the Ni and Co leaching efficiencies are 97.4% and 98.8%, respectively, and most of the ferrous ions are oxidized to ferric ions and then precipitated so that the leaching efficiency of unwanted Fe is only 4.7%. The practicality of the acid-free process is reflected in the selective atmospheric water leaching, which uses air or oxygen as oxidants without additional leaching agents. Technoeconomic analysis shows that the acid-free process provides excellent economic and environmental advantages, indicating a low carbon footprint process for the selective leaching of Ni and Co from NSC.

Results
Acid-free and selective leaching promoted by mechanical activation
The crystal structure of a Ni-bearing sulfide involves the closest packing of S, with Fe occupying tetrahedral or octahedral spaces and Ni or Co replacing part of the Fe in the form of isomorphism (Fig. 1a). As a result, the oxidation of sulfur is crucial to the leaching of metal ions. Previous studies have shown that the main chemical reactions during the NSC leaching process can be described with the following equations (Supplementary Figs. 3–5 elucidates the outcomes of an analysis grounded in reaction thermodynamics)[47,48]:

$$Fe_{0.9}S + 0.45O_2 + 1.8H^+ \rightarrow 0.9Fe^{2+} + S + 0.9H_2O \quad (1)$$

$$0.125Fe_{4.5}Ni_{4.5}S_8 + 0.56O_2 + 2.24H^+ \rightarrow 0.56Ni^{2+} + 0.56Fe^{2+} + S + 1.12H_2O \quad (2)$$

$$Fe_{0.9}S + 1.95O_2 + 0.1H_2O \rightarrow 0.9Fe^{2+} + SO_4^{2-} + 0.2H^+ \quad (3)$$

$$0.125Fe_{4.5}Ni_{4.5}S_8 + 2.06O_2 + 0.24H^+ \rightarrow 0.56Ni^{2+} + 0.56Fe^{2+} + SO_4^{2-} + 0.12H_2O \quad (4)$$

$$Me_xS + \frac{x+3}{2}O_2 + (1-x)H_2O \rightarrow xMe^{2+} + SO_4^{2-} + (2-2x)H^+ \quad (5)$$

In accordance with the stoichiometric relationships presented in Eqs. (1–4), the oxidation of sulfides to sulfate proceeds via an acid-generation pathway only when a specific metal-to-sulfur ratio is attained. This regulation can be summarized with Eq. (5), which indicates that when the ratio of metal (Me) to sulfur (S) expressed as Me/S is less than unity ($0 < x < 1$), the oxidation reaction leads to acid production. Conversely, when the ratio exceeds unity ($x > 1$), the oxidation reaction is associated with acid consumption. Consequently, the different coordination states of sulfur have a significant effect on the oxidation process. This work demonstrates that the selective oxidation of NSC was achieved by inducing mechanical activation, resulting in the acid-free leaching of NSC under atmosphere. Acid-free and selective leaching was induced with mechanical activation, and the leaching efficiencies for Ni, Co, Cu and Fe were 97.4%, 98.8%, 91.4% and 4.7%, respectively (Fig. 1h). However, the leaching efficiencies of Ni and Co were only 6.7% and 4.4%, respectively, without mechanical activation (Fig. 1g). As shown in Fig. 1i, the Ni and Co solution obtained via acid-free leaching undergoes conventional impurity removal and extraction processes (Supplementary Fig. 17), culminating in the production of battery-grade Ni and Co sulfate (Supplementary Fig. 18). Subsequently, NCM523 cathode material was synthesized by the conventional co-precipitation and calcination using the prepared Ni and Co sulfate (Supplementary Fig. 19). As shown in Supplementary Fig. 20, the synthesized NCM523 cathode material has comparable cycle stability and rate performance to commercial NCM523 cathode material.

Subjected to mechanical force, NSC particles are rapidly broken along the cleavage plane, providing the potential to generate sulfur species with reduced coordination (Fig. 1b)[49]. Undercoordinated sulfurs, characterized by their heightened reactivity[50,51], are the key to acid-free leaching under atmosphere. As shown in Fig. 1c, the proportion of undercoordinated sulfur (S^{1-}) remained above 20% after mechanical activation, while the ratio of iron-to-sulfur decreased from 1.07 to 0.83 with increasing activation time (Fig. 1e). Notably, mechanical activation significantly changed the XPS peak positions of the S 2p (Fig. 1f) and Fe 2p (Supplementary Fig. 6b) XPS peaks. As the activation time increased, the peak positions of S^{2-} and S^{1-} shifted toward low binding energies by 0.36 eV and 0.20 eV, respectively, while Fe(II) at the center of octahedra or tetrahedra composed of S shifted toward high binding energies by 0.43 eV. It has been reported that this variation in binding energy is associated with the change in surface electron density[52,53], meaning that in the lattice the electron density of S increases after activation while the electron density of Fe decreases. Therefore, mechanical activation enhances the polarity of the Fe–S bond and increases its oxidation reaction activity.

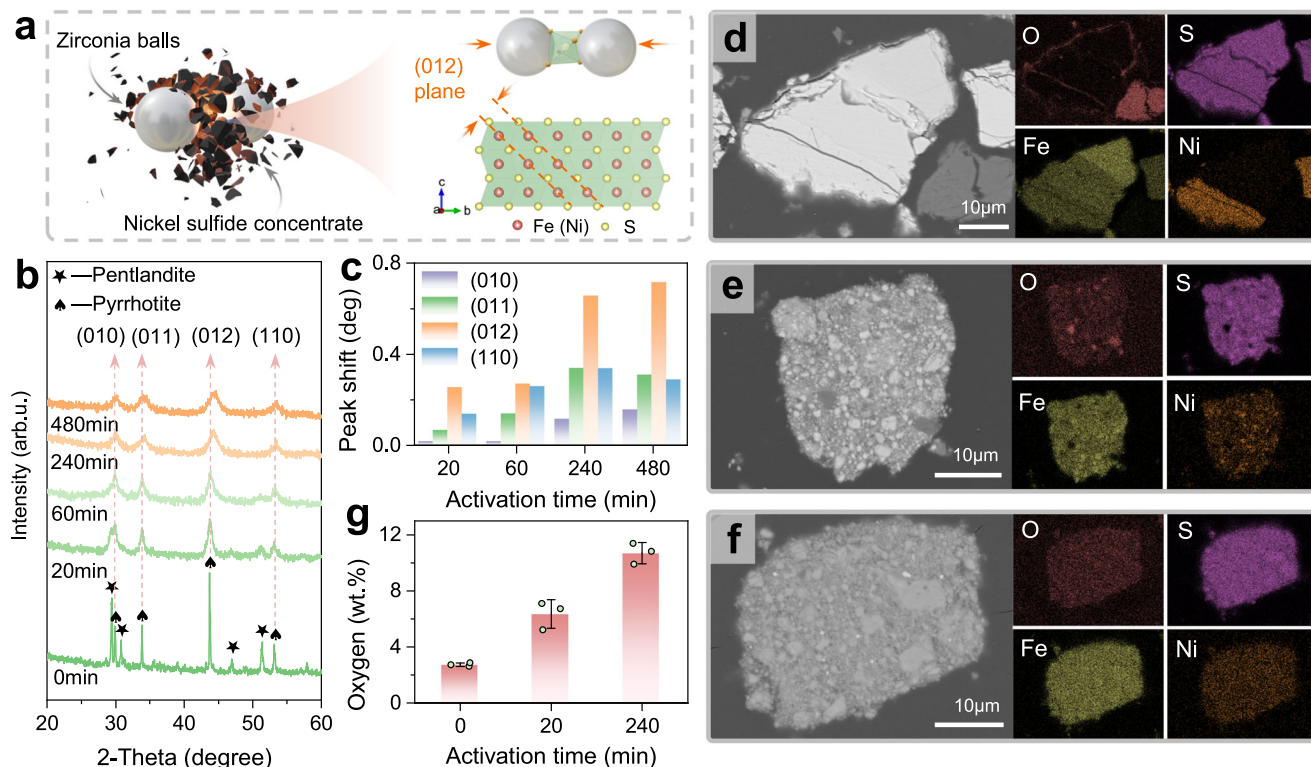### Structural evolution of activated NSC
The edges of the fractured surfaces of NSC particles due to mining crushing are clearly visible (Supplementary Fig. 7a). After 20 min of activation, the edges of the NSC particles are destroyed (Supplementary Fig. 7b). The median particle (D50) size of the NSC particles decreased from 29.6 μm to 12.4 μm (Supplementary Fig. 7d), the BET surface area increased sharply from 0.8 m^2 g^{-1} to 8.3 m^2 g^{-1}
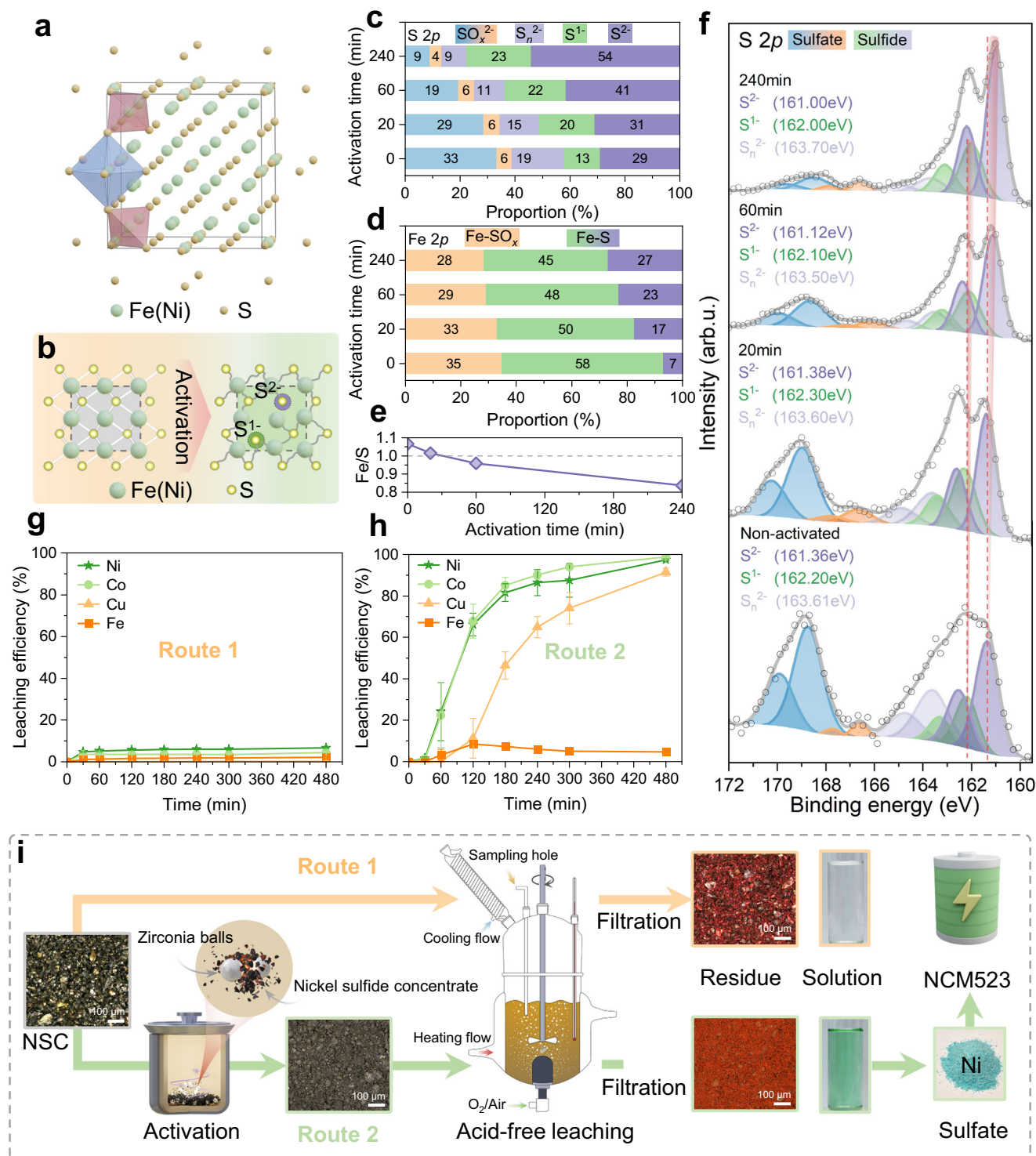
Fig. 1 | Acid-free and selective leaching promoted by mechanical activation.
a Crystal structure of $Ni_{4.5}Fe_{4.5}S_8$, in which iron (Fe) occupying the tetrahedral or octahedral spaces formed by the closest packing of sulfur (S). **b** Schematic diagram of the bonding relationships in the Ni sulfide concentrate (NSC) before and after activation, in which the square dotted line frame represents the lattice frame, and the S atoms shaded in purple and green circles represent saturated sulfur (S^{2-}) and undercoordinated sulfur (S^{1-}), respectively. X-ray photoelectron spectroscopy (XPS) data showing the compositional proportions of (**c**) various sulfur species,

d various iron species, and (**e**) Fe/S in different samples. **f** S 2p XPS spectra of NSC activated for 0, 20, 60, and 240 min. Leaching efficiency of Ni, Co, Cu and Fe from (**g**) nonactivated NSC and (**h**) 240 min activated NSC. The error bars in **g**, **h** reflect the standard deviations from three individual experiments. **i** Flowsheet of the acid-free leaching process, in Route 1, the nonactivated NSC is difficult to leach, while in Route 2, the activated NSC undergoes efficient leaching to obtain a nickel-containing solution, which is ultimately prepared into $LiNi_{0.5}Co_{0.2}Mn_{0.3}O_2$ (NCM523) cathode material. Source data are provided as a Source Data file.

Fig. 2 | Structural evolution of activated NSC. a Schematic diagram of the mechanical activation. **b** X-ray diffraction (XRD) analysis of activated Ni sulfide concentrate (NSC). **c** Peak shifts of the diffraction peaks of NSC with different activation times. Cross-sectional scanning electron microscope (SEM) images and energy dispersive spectroscopy (EDS) analysis of (**d**) nonactivated NSC, (**e**) NSC activated for 20 min, (**f**) 240 min, and (**g**) the oxygen content of the cross-section. The error bars in **g** represent the standard deviations from three parallel measurements. Source data are provided as a Source Data file.

(Supplementary Fig. 7f), and the apparent reaction rate constant of Ni increased by 477 times greater than that of nonactivated NSC (Supplementary Table 2). As mechanical activation progresses, small particles aggregate due to electrostatic attraction (Supplementary Fig. 7c), increasing the D50 size to 13.8 μm at 240 min of activation. Additionally, the squeezing effect of the grinding ball welds the particles together, increasing the compactness of the agglomerates and thus reducing the BET specific surface area of NSC to 6.1 m² g⁻¹ at 240 min of activation. However, as the activation time increased from 20 min to 240 min, the apparent reaction rate constant of Ni still increased (Supplementary Table 2), inconsistent with the conventional understanding that the BET specific surface area and apparent reaction rate constant are positively correlated[54,55]. This is because mechanical activation involves two functions: morphological reconstruction and structural disorder (Fig. 2a)[42]. As shown in Supplementary Fig. 14, the overlapping effect of the BET specific surface area and structural disorder of the activated NSC particles was confirmed. This means that after 20 min of activation, the negative effect of further activation leading to a decrease in the BET specific surface area on Ni leaching is offset by the positive effect of structural disorder. Therefore, for NSC activated for 240 min the increase in the apparent reaction rate constant is dominated by structural disorder. As shown in Fig. 2b, c, the structural disorder of 240 min activated NSC is revealed by the maximum peak shift of the (012) planes of pyrrhotite toward high angles. According to the Bragg equation, the spacing d between the (012) planes decreases, meaning that the crystal planes where metal atoms such as Ni or Co are located have the largest distortion, thus increasing the apparent reaction rate constant of Ni and Co. Up to 480 min of activation, the XRD diffraction peak of the (012) planes shifted to a high angle by only 0.06°, and the diffraction peaks of the (011) and (110) planes even shifted to low angles (Fig. 2c), causing the apparent

reaction rate constant of Ni to stop increasing (Supplementary Table 2). Moreover, the Ni distribution of the NSC particles after mechanical activation can be visualized through EDS cross-sectional analysis. After 20 min of activation, blocky Ni-rich particles are broken (Fig. 2d, e), but some Ni-rich particles remain. These Ni-rich particles were further broken after 240 min of activation, with Ni well distributed throughout the aggregates (Fig. 2f). In summary, although the BET surface area of the NSC particles decreased after activation for more than 20 min, the structural disorder continued, and the Ni-rich particles were further broken and subdivided, resulting in an apparent reaction rate constant for Ni after 240 min of activation was 2322 times greater than that of nonactivated NSC. Therefore, structural disorder is considered a major factor for Ni leaching of mechanically activated NSC.

XPS depth profiling was performed to understand the evolution of the atomic fractions and the chemical state of the activated NSC. As shown in Fig. 3d, the S 2p spectra can be split into groups of under-coordinated sulfur (S¹⁻) and saturated sulfur (S²⁻) peaks at 162.0 eV and 161.3 eV, and the surface (0 s) spectrum is the same as in Fig. 1f, with a weak peak corresponding to sulfate at 168.8 eV[56]. The sulfate peak disappeared after etching for 60 s, indicating that the complete oxidation of sulfur occurred on the near surface of the activated NSC particles only, possibly caused by the particles being exposed to air. The oxygen reactivity of the activated NSC can also be confirmed by EDS analysis. As shown in Fig. 2g, after activation for 240 min the oxygen content in the cross-section of the NSC particle aggregate increased from 2.7% to 10.7%. As shown in Fig. 3c, the O 1 s surface (0 s) spectrum can be split into three peaks corresponding to gangue silicate (O-Si)[57,58], metal hydroxide (OH⁻) and metal oxide(O²⁻)[59,60] near 532.8 eV, 531.8 eV and 529.9 eV, respectively. After etching for 300 s, the oxide surface of the NSC particle was removed, and the peak at
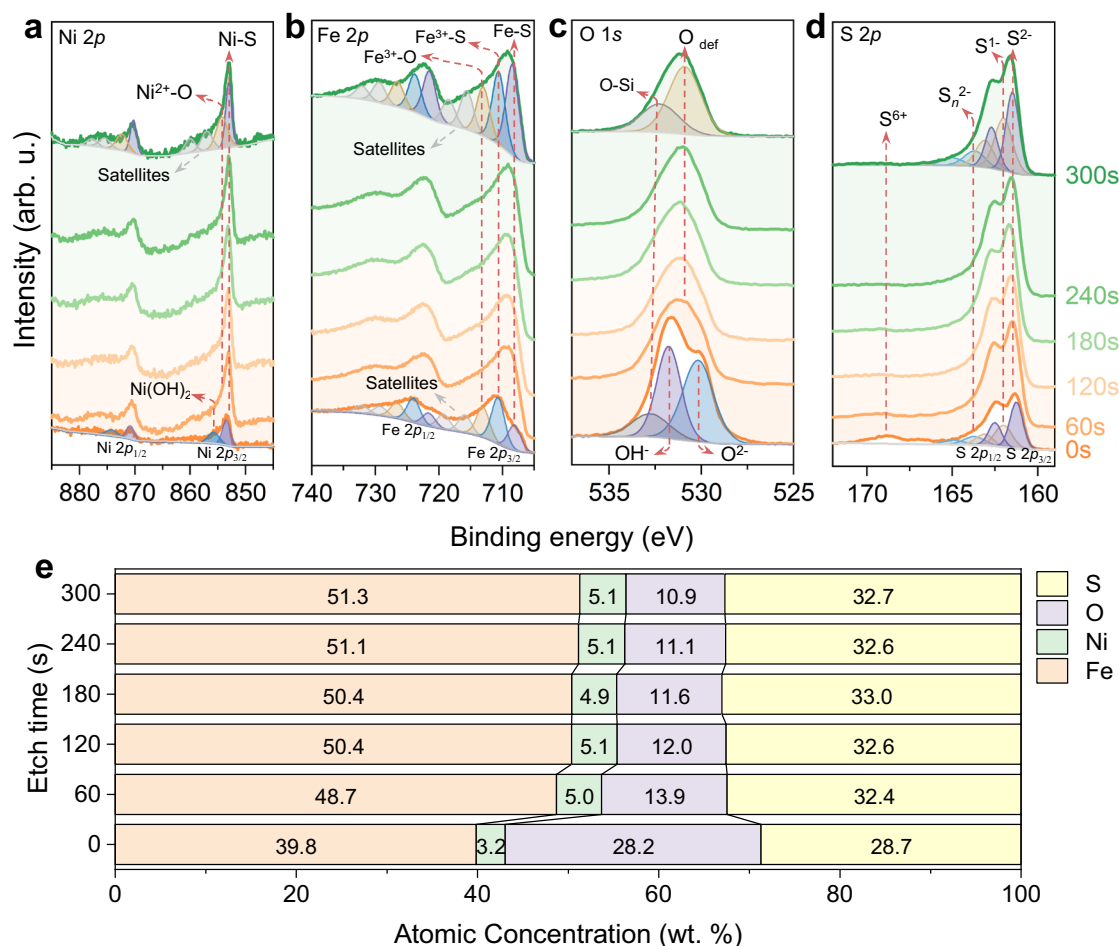
Fig. 3 | Chemical state evolution of activated NSC. a Ni $2p$, **b** Fe $2p$, **c** O $1s$ and **d** S $2p$ detail spectra for the x-ray photoelectron spectroscopy (XPS) depth profile of 240 min activated Ni sulfide concentrate (NSC), and (**e**) evolution of atomic fractions for S, O, Ni and Fe calculated from the depth profile. The time labels on the right side of **d** represent the etching time of XPS depth sputtering. Source data are provided as a Source Data file.

approximately 530.9 eV was attributed to defective oxygen (O $_{def}$)[61,62]. This is the result of oxygen atoms adsorbing on Ni and Fe vacancies in the process of structural disorder caused by mechanical activation[63]. As shown in Fig. 3b, the Fe $2p$ surface (0 s) spectrum can be split into five groups of peaks. The three groups of peaks at 708.1 eV, 710.7 eV and 713.1 eV are attributed to ferrous sulfide (Fe-S), ferric sulfide (Fe^{3+}-S) and oxide (Fe^{3+}-O), respectively. The other two groups are satellite peaks at 715.9 eV and 719.3 eV[49,59,64]. The Fe species of the bulk (300 s) NSC particles are consistent with those of the surface (0 s) but the proportion of sulfide inside is greater than that on the surface. As mentioned above, this phenomenon is caused by surface oxidation upon exposure to air. As shown in Fig. 3a, the Ni $2p$ surface (0 s) spectrum can be split into two groups corresponding to Ni hydroxide (Ni (OH)$_2$) and sulfide (Ni-S) near 855.8 eV and 853.5 eV[61,65]. The surface Ni hydroxide is formed by the reaction of air-exposed bulk (300 s) Ni oxide (Ni^{2+}-O), with a peak at 854.3 eV[62]. Thus, the evolution of the chemical state of activated NSC particles consists of the surface S species becoming partially completely oxidized due to air exposure while the bulk S species maintain their reduced state and have high oxidation activity. The surface metal species such as Ni oxide react with air to form hydroxides and the bulk Ni and Fe species were partially oxidized. Considering that the metal atomic sites in sulfides, such as Fe atoms, are the preferred sites for oxygen contact reactions[66,67], the oxide species of Fe and Ni in the bulk of activated NSC particles are possibly derived from the metal defect sites generated by mechanical

activation and adsorbing oxygen in the grinding tank. As shown in Fig. 3e, from the surface to the bulk of the particles (Etch 0–300 s) oxygen content decreases, while the content of S, Ni and Fe contents increase and then stabilize. Therefore, the outside-in oxidation characteristics of the activated NSC particles were confirmed by the evolution of the atomic fractions and chemical states.

Leaching behavior of activated NSC
As a proof of concept, a two-step process was established for the selective leaching of Ni from NSC, in which mechanical activation can be easily achieved by ball milling equipment, and subsequent leaching was performed in a custom-designed aeration reactor. Figure 4a, b shows the effects of the activation time on the leaching efficiency of Ni and Fe. Increasing the activation time can improve the Ni leaching efficiency and reduce the Fe leaching efficiency, thus promoting the selectivity of the leaching process. The three key parameters of mechanical activation, activation time, ball-to-powder ratio (Supplementary Fig. 8d), and ball milling speed (Supplementary Fig. 8e), can be unified by Eq. (7) for the mechanical energy (E) input into the NSC powder system. As shown in Fig. 4c, in the range of 0 to 350 kJ, the leaching efficiency of Ni, Co, and Cu continued to increase with increasing mechanical energy, while the leaching efficiency of Fe increased and then decreased, with a maximum leaching efficiency of 15% and a minimum pH of 1.8 near 150 kJ. When the leaching rate of Fe is faster than the precipitation rate during the leaching process, the
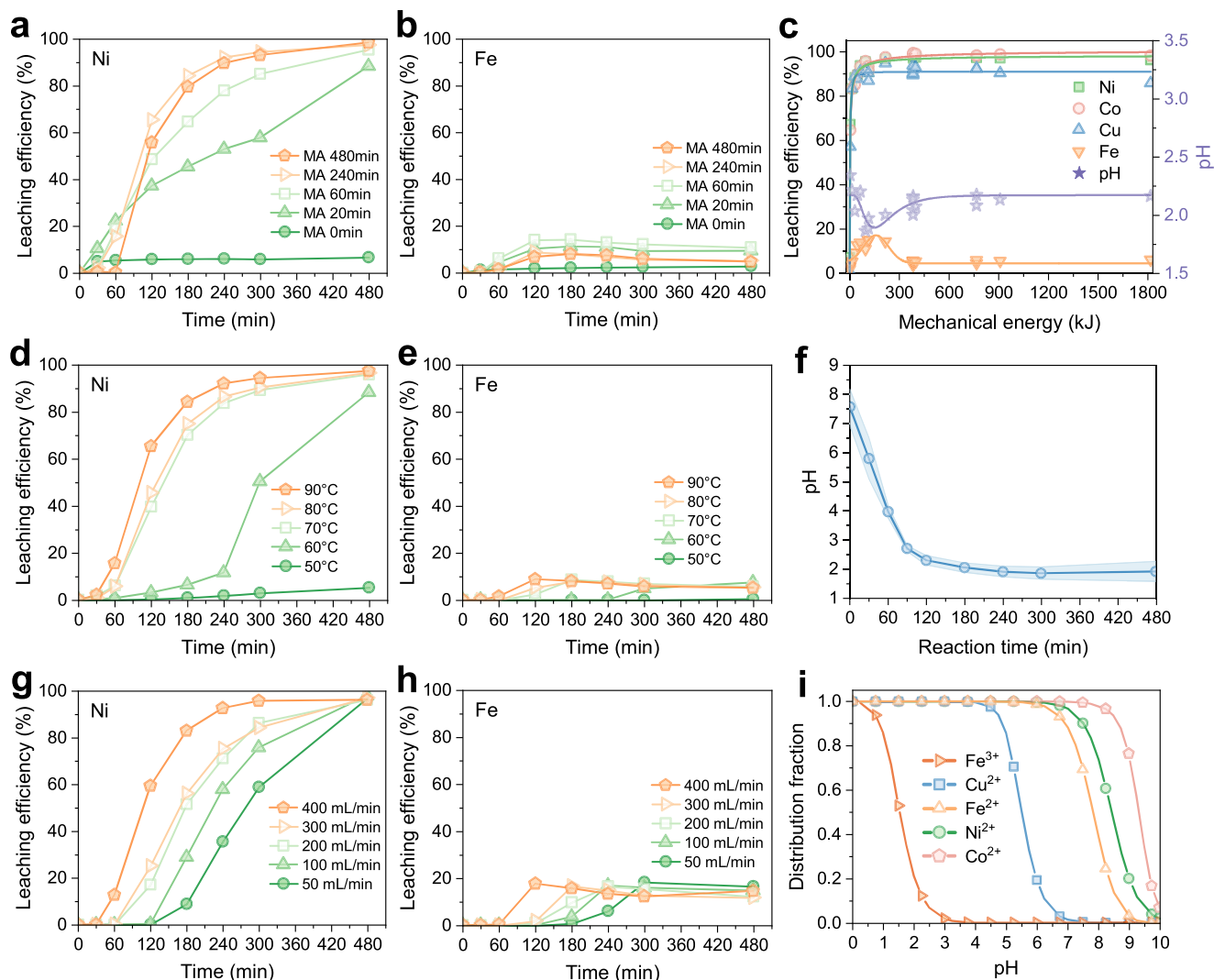
Fig. 4 | Leaching behavior of activated NSC. Effects of activation time (**a**, **b**), mechanical energy (**c**), reaction temperature (**d**, **e**) and oxygen flux (**g**, **h**) on metal leaching. **f** pH of the solution during the acid-free leaching process. The lines in **c** serve only as a visual guide to show the distribution of the data points. The shaded error bands in **f** reflect the standard deviations from three individual experiments. **i** Distribution of Ni, Co, Cu and Fe ions in aqueous solutions with different pH values (Calculated using Visual MINTEQ 3.1 software). Source data are provided as a Source Data file.

leaching efficiency of Fe increases, and vice versa. The precipitation of Fe depends on the pH of the solution. Figure 4i shows that at pH 2.3, less than 10% of the Fe^{3+} remains in the solution. As mentioned in the previous section, the undercoordinated sulfur in NSC generated by activation is oxidized to sulfuric acid during leaching, causing the pH of the solution to drop from 7.5 to 2.3 after 120 min of leaching (Fig. 4f), resulting in an acid-free leaching process under atmosphere. The leaching of activated NSC is temperature dependent (Fig. 4d), and a shrinking core model was established to describe the kinetics of acid-free leaching (Supplementary Fig. 11). For the 240 min activated NSC, Ni leaching at lower temperatures (50–70 °C) exhibited two distinct stages (Supplementary Fig. 12a). The first stage demonstrated slow kinetics with an apparent free energy of 94.6 kJ mol^{-1} (Supplementary Fig. 12g), indicating Ni leaching controlled by the surface reaction rate. This originated from the initial leaching solution containing only water and air, where the metal leaching relied on acid-generating oxidation of undercoordinated sulfur, which is a rate-determining step under low-temperature conditions. Upon elevating the temperature to 80–90 °C, the inhibitory effects of the first stage were essentially eliminated, and the apparent free energy of Ni leaching from 240 min

activated NSC is 11.3 kJ mol^{-1} (Supplementary Fig. 12d), which is half the 20 min activated NSC (25.6 kJ mol^{-1}) (Supplementary Fig. 12k), indicating Ni leaching controlled by the gray layer diffusion. Cross-sectional SEM-EDS analysis of leached particles revealed that 240 min activated NSC surfaces developed a porous iron oxide layer (2–4 μm) after 60 min reaction at 90 °C, confirming the kinetic analysis conclusion that Ni leaching controlled by the residual layer diffusion (Supplementary Fig. 13). Therefore, increasing the oxygen transfer rate can significantly accelerate the Ni leaching process (Fig. 4g).

In addition, the oxidation-reduction potential (ORP) is also crucial for the oxidation reaction in NSC leaching[34,68]. Previous studies have shown that the use of oxygen microbubble aeration produces hydroxyl radicals, which significantly increases the ORP (Supplementary Fig. 9a)[69–71]. As shown in Supplementary Fig. 9b, DMPO-OH was detected in the reactor aerated with a 5 μm aperture for 20 min, confirming the formation of hydroxyl radicals. Under the same conditions, no obvious signal was detected with aeration with a 6 mm aperture (Supplementary Figs. 9c, 10). Therefore, microbubble aeration can improve the leaching efficiency of nickel. As shown in Supplementary Fig. 9d, the Ni leaching efficiency of 20 min activated NSC with 5 μm aeration was
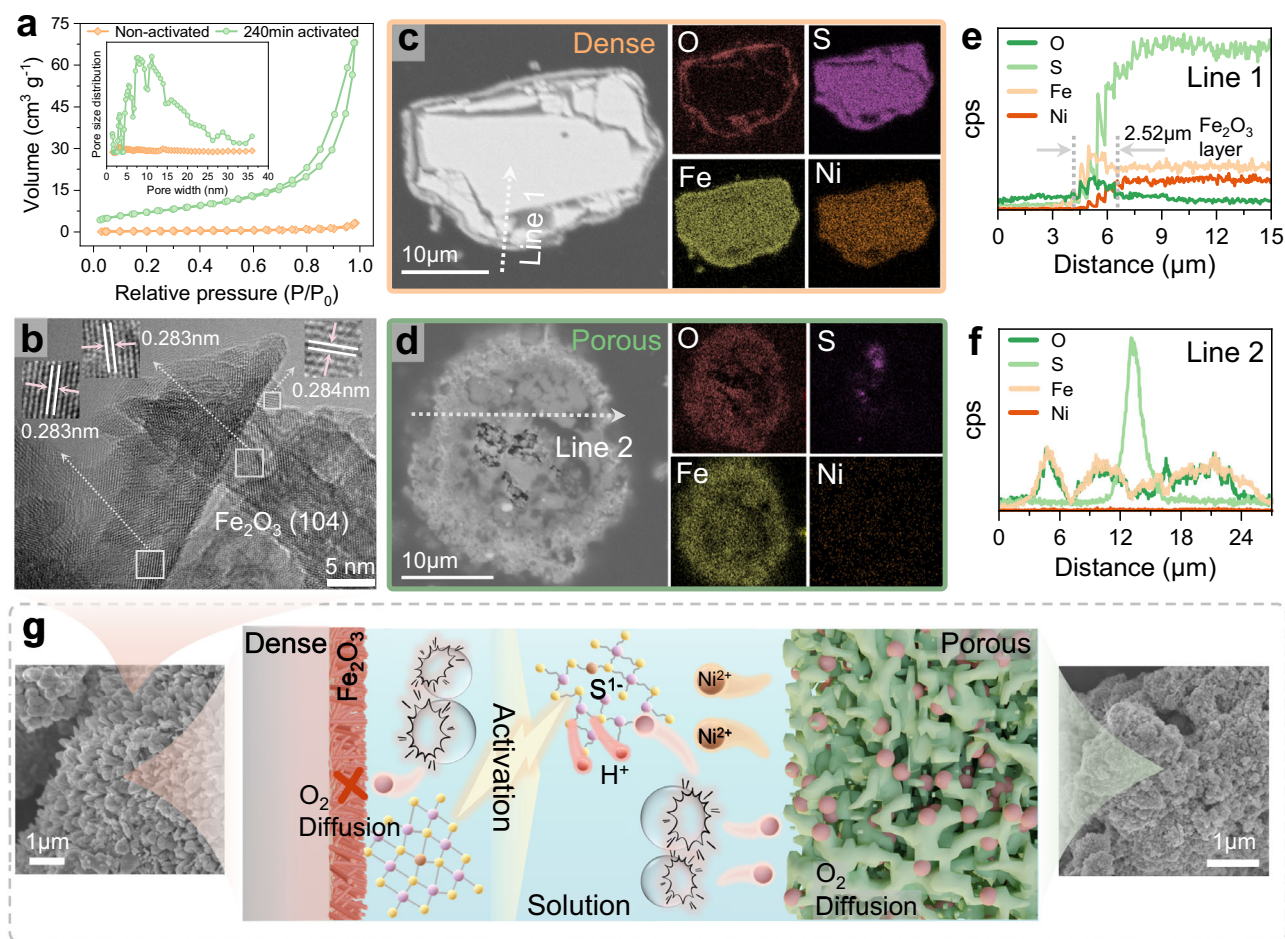
Fig. 5 | Proposed mechanism for acid-free and selective leaching. a N_2 adsorption-desorption isotherms of the leaching residue. **b** High resolution transmission electron microscope (HRTEM) image of the leaching residue of non-activated Ni sulfide concentrate (NSC). Energy dispersive spectroscopy (EDS) line scanning and surface scanning of the cross-sections of the leaching residues of (**c**, **e**) nonactivated and (**d**, **f**) 240 min activated NSC. **g** Schematic diagram of the proposed acid-free and selective leaching mechanism. The non-activated NSC surface formed a dense hematite layer hindering oxygen diffusion, whereas 240 min activated NSC developed porous amorphous iron oxides. Oxygen permeated through these pores to access undercoordinated sulfur sites within particles, enabling in situ acid generation via sulfur oxidation. Source data are provided as a Source Data file.

15.1% greater than that with 6 mm aeration, and the difference in leaching efficiency decreased as the activation time increased. As mentioned above, mechanical activation improves the oxidation reactivity of NSC, reducing the dependence of the NSC leaching reaction on a high ORP. Thus, when air was used instead of pure oxygen as the oxidant to leach 240 min of activated NSC, the leaching efficiency of Ni and Co was also above 92% (Supplementary Fig. 9e).

Mechanism of acid-free and selective leaching

To further reveal the oxidation characteristics of NSC in aqueous solution, the leaching residue was fixed in resin, which was subsequently polished to expose the inside of the particles. Figure 5c, d shows the surface mappings of the cross-sectional profiles for the non-activated and 240-minute activated NSC particles. The leaching of nonactivated NSC for 8 h led to the formation of an Fe oxide layer with a thickness of approximately 2.52 μm on the particle surface (Fig. 5e). This layer was predominantly composed of rod-shaped hematite (Supplementary Fig. 15a, d). Upon subjecting the 240-minute activated NSC particles to acid-free leaching for 8 h, complete oxidation was achieved (Fig. 5f), with the leaching residue primarily comprising elemental sulfur and iron oxides (Supplementary Figs. 15b, 16). The elemental sulfur was readily extractable with tetrachloroethylene, while the residual iron oxide exhibited an amorphous structure devoid of distinct XRD peaks

(Supplementary Fig. 15c). Figure 5a presents the N_2 adsorption-desorption isotherms for the 8-hour leaching residues of both the nonactivated NSC and 240-minute activated NSC. The residue from the 240-minute activated NSC sample exhibited a type IV isotherm with a pronounced H3 hysteresis loop, indicative of a prevalent and well-distributed mesoporous structure. The corresponding average pore diameter and specific surface area for this residue were determined to be 9.52 nm and 25.65 m^2 g^{-1}, respectively (Supplementary Fig. 15f). In stark contrast, the 8-hour leaching residue of the nonactivated NSC manifested a significantly lower specific surface area of 0.95 m^2 g^{-1} and lacked a discernible pore structure, suggesting a dense morphology.

Figure 5g shows that as a consequence of the acid-free leaching process a compact layer of rod-shaped crystalline hematite formed on the surface of the nonactivated NSC. The formation of hematite at the oxidatively active sites results in the deactivation of oxidation, with the diffusion of oxygen being impeded by the dense hematite layer. This barrier effectively retards the leaching of Ni. In contrast, the 240-minute activated NSC exhibited a fourfold increase in specific surface area post leaching attributable to the precipitation of iron, which congregated to form porous, amorphous iron oxides. Oxygen permeates through these pores, reaching the undercoordinated sulfur sites within the particles and in situ acid generation to sustain the requisite acidity in the solution for the leaching of Ni.
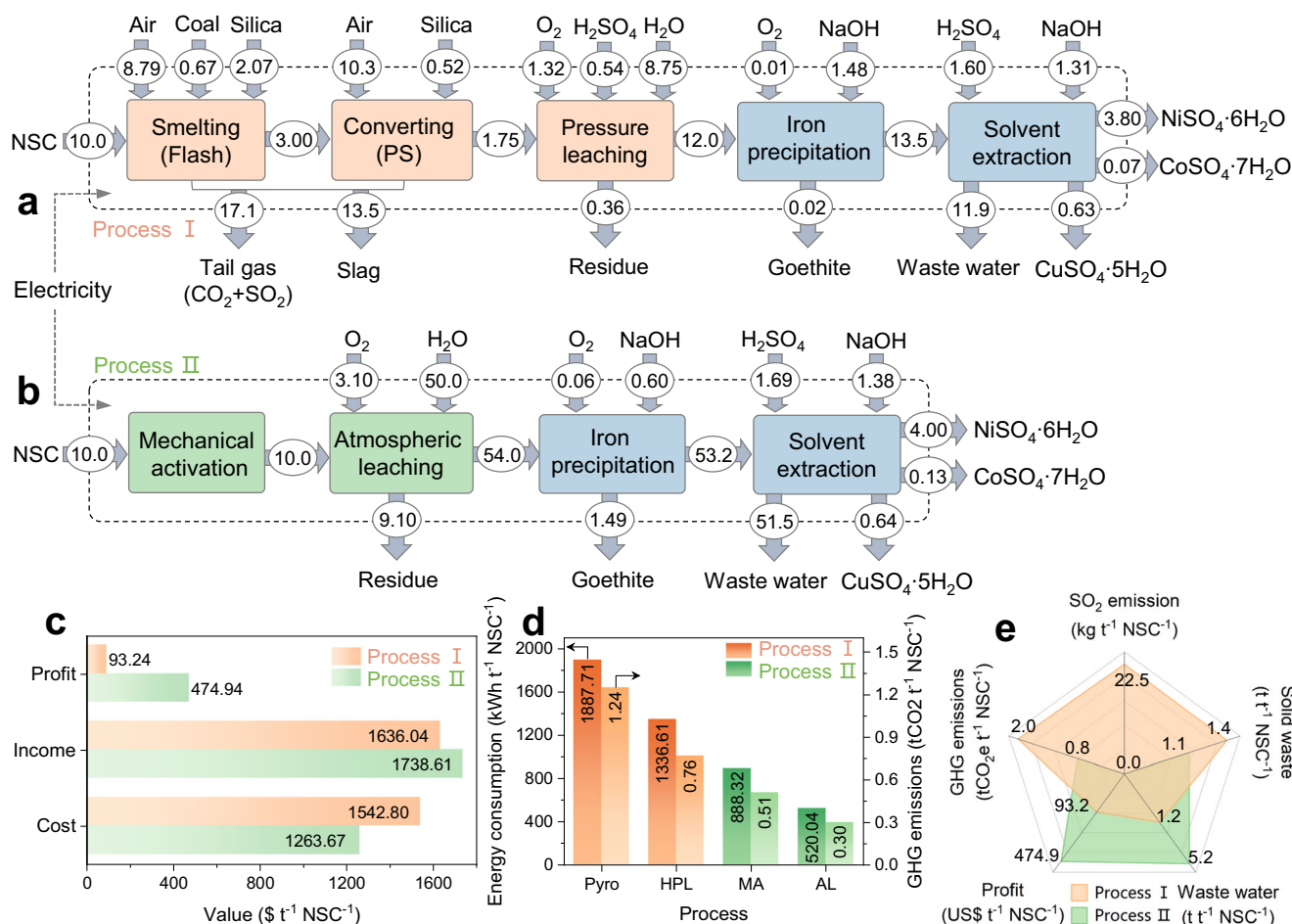
Fig. 6 | Technoeconomic assessment. Material flow analysis of (**a**) the traditional pyrometallurgical-hydrometallurgical process and (**b**) acid-free atmospheric leaching process. The units of the numbers in **a**, **b** are tons. **c** Economic and (**d**) energy consumption analysis of the two processes. In Process I, Pyro stands for pyrometallurgical process including smelting and converting, and HPL stands for pressure leaching. In Process II, MA stands for mechanical activation, and AL stands for atmospheric leaching. **e** Comprehensive comparison of the two processes. Source data are provided as a Source Data file.

Technoeconomic assessment

Technoeconomic assessment (TEA) was conducted to evaluate the practicality of the acid-free atmospheric leaching process (Process II) compared with the traditional pyrometallurgical hydrometallurgical combined process (Process I). The specific calculations of the TEA are provided in the Supplementary Tables 3–5. Taking the treatment of 10 t NSC as an example (Fig. 6a, b), the production of Ni, Co, and Cu sulfate by the Process I is 3.80 t, 0.07 t, and 0.63 t, respectively, while the production of Ni, Co, and Cu sulfate by the Process II is 4.00 t, 0.13 t, and 0.64 t, respectively, indicating a notable 85.71% increase in the production of Co sulfate compared with Process I. As shown in Fig. 6c, owing to increased Ni, Co, and Cu sulfate production and the reduced reagent consumption, the profit of Process II is 474.94 $ t^{-1} NSC, which is 5.1 times greater than that of Process I.

The core difference between Processes I and II is the reaction path of Ni from the solid phase into the solution. In Process I, Ni is treated with high-temperature smelting and pressure leaching, while in Process II, Ni is leached directly at atmospheric pressure. Figure 6d displays the energy consumption of different processes, revealing that the energy consumption of pyrometallurgical smelting constitutes 58.55% of the total energy consumption of Process I. The energy consumption of Process II is 1408.36 kWh t^{-1} NSC, 1815.96 kWh t^{-1} NSC less than Process I and involves no direct combustion of fossil energy. The resulting reduction in greenhouse gas (GHG) emissions is 1.19 tCO$_2$ t^{-1} NSC, which is 59.5% lower than for Process I. Notably, Process II has

almost no sulfur dioxide emissions and reduces solid waste by 23.70%. Although relatively more wastewater is generated, the wastewater is easy to treat and recycle due to the absence of additional leaching agents in the leaching process (Fig. 6e). Overall, Process II is significantly superior to Process I in terms of energy consumption, exhaust gas and slag emissions, and economic benefits. It is a promising process with great potential for application.

Discussion

Inspired by the oxidation of undercoordinated sulfur to sulfuric acid, we presented an acid-free and selective NSC atmospheric leaching process. Owing to the structural disorder caused by mechanical activation, over 20% of the undercoordinated sulfur was formed in the NSC. During atmospheric leaching of activated NSC, undercoordinated sulfur is oxidized in situ to sulfuric acid, which facilitates the in-situ leaching of metals. The oxygen microbubbles collapsed in the solution to form hydroxyl radicals, increasing the oxidation potential and thereby improving the leaching efficiency and selectivity of Ni and Co. Under optimized operating conditions, the Ni and Co leaching efficiencies are 97.4% and 98.8%, respectively, and most of the ferrous ions are oxidized to ferric ions and then precipitated so that the leaching efficiency for unwanted Fe is only 4.7%. When oxygen was replaced with air, the leaching efficiency of Ni and Co was also above 92.0%.

Efficient leaching of Ni and Co under atmospheric pressure was achieved without additional leaching agents. Technoeconomic

analysis revealed that compared with the traditional pyrometallurgical-hydrometallurgical process, the acid-free process reduces energy consumption by 56.3%, carbon dioxide emissions by 59.5%, sulfur dioxide emissions by almost 100%, and solid waste by 23.7%. In summary, the acid-free process offers substantial economic and environmental advantages. This method is expected to be applied to zinc and copper sulfide concentrates (Supplementary Figs. 21, 22), providing a sustainable alternative for processing complex sulfide resources.

Methods
Chemicals and materials
Nickel sulfide concentrate was provided by a Chinese mineral resource development company (Qinghai Yellow River Mining Co., Ltd.). The relevant mineral characterization was presented in the Supplementary Table 1, Supplementary Figs. 1, 2. The aqua regia used to dissolve the samples is prepared with hydrochloric acid (Superior pure, Sinopharm Chemical Reagent Co., Ltd.) and nitric acid (analytical pure, Sinopharm Chemical Reagent Co., Ltd.) in a volume ratio of 3:1. Ultrapure oxygen gas (purity > 99.999%) was obtained from Beijing Qianxi Gas Co., Ltd. Commercial NCM523 cathode material was purchased from Kejing Star Technology Co., Ltd., Shenzhen, China. All solutions were made with ultrapure water (Milli-Q Direct 8, Millipore).

Extraction process
Mechanical activation was performed in a planetary ball mill facility (PULVERISETTE-7, Fritsch, Germany) equipped with two 45 ml zirconia jars. The effects of the ball-to-powder mass ratio (5, 10, 20, 30, or 40 g/g), mill rotation speed (200, 300, 400, 600, or 800 rpm), and rotation time (20, 60, 240, or 480 min) on the metal leaching efficiency were investigated systematically. To prevent the equipment from overheating, the ball mill was operated continuously for 20 min at 10 min intervals. The final mechanically activated nickel sulfide concentrate samples were collected for subsequent leaching experiments.

The atmospheric acid-free leaching experiment was carried out in a custom-designed aeration reactor. First, the activated ore powder with a specific weight was weighed and put into the reactor, and then 300 ml of ultrapure water was added. After the reactor was assembled, hot water and cold water were introduced. When the thermometer in the reactor reaches the specified value, the oxygen (air) flow meter valve (the zero point at the beginning of the reaction) is opened, the specified flow of oxygen (air) is passed into the solution through a specially designed microporous aeration head (pore 5–10 μm) in the form of microbubbles. Sampling is performed as needed during the reaction process and the reaction time is strictly recorded. The effects of temperature (50, 60, 70, 80 and 90 °C), the liquid–solid ratio (10, 20, 30, 50 and 100 mL/g) and the oxygen flux (50, 100, 200, 300 and 400 mL/min) on the leaching efficiency of the main metal elements were investigated systematically.

The leaching efficiency of metal elements (R_i), was calculated via Eq. (6):

$$R_i = m_{iL}/(m_{iR} + m_{iL}) \times 100\% \qquad (6)$$

where m_{iL} is the mass of "i" in the leaching solution, m_{iR} is the mass of "i" in the leaching residue, and "i" represents Ni, Co, Fe, or Cu.

The mechanical energy involved in the mechanical activation was calculated via Eq. (7)[39]:

$$\frac{E}{m_p} = -\varphi_b N_b m_b t \left(W_P - W_v \right) \left[\frac{w_v^3 \left(R_v - \frac{d_b}{2} \right)}{W_P} + W_P W_v R_p \right] \left(R_v - \frac{d_b}{2} \right) / 2\pi m_p \qquad (7)$$

where, E is the mechanical energy involved in the ball milling process; m_p is the mass of the materials in the pot; φ_b is the vial filling factor; N_b is the number of balls; m_b is the mass of a ball; t is the rotation time; W_P and W_v are the mill speed and angular velocities of the disk and vial, respectively; R_v and R_p are the radii of the vial and disk, respectively; and d_b is the ball diameter.

Characterization
To obtain a more accurate content for the metal elements the leaching residue was dissolved in aqua regia (HCl : HNO₃ = 3:1, v/v) and filtered, then the filtrate was diluted multiple times. The element content was analyzed using inductively coupled plasma–optical emission spectrometry (ICP–OES; Agilent 5800 VDV, Agilent Technologies, Inc., Malaysia). The crystal structure and phase composition of the nickel sulfide concentrate were characterized using X-ray diffraction (X'pert PRO, PANalytical) with Cu Kα radiation. The data were collected using step scanning with a scanning speed of 10°/min and a scanning angle (2θ) of 5–90°. X-ray photoelectron spectroscopy (XPS, ESCALAB 250Xi spectrometer, Thermo Scientific) was subsequently used to explore the surface phase formation and transformation behavior before and after ball milling or leaching. The excitation source was an Al Kα X diffraction source and the binding energy was corrected using the C 1 s peak of hydrocarbons at 248.8 eV. Furthermore, the morphologies of the activated samples were observed using a field emission scanning electron microscope (FESEM; JSM-7610F, JEOL, Ltd., Japan) equipped with an energy dispersive spectrometer. Additionally, the specific surface areas of the activated samples were measured with a nitrogen gas adsorption analyzer (ASAP 2020 HD88 AS, Micromeritics Instrument Corporation, USA) employing the Brunauer-Emmett-Teller (BET) method. TEM analysis was performed with transmission electron microscopy (TEM, JEOL JEM2010F, Japan). Finally, the Gibbs free energy change during the possible chemical reactions were calculated using HSC 10.0 software (Metso Outotec, Finland).

Data availability
The source data presented in this study have been deposited in the Figshare database under access code https://doi.org/10.6084/m9.figshare.28816484. All raw data generated during the current study are available from the corresponding authors upon request. Source data are provided with this paper.

References
1. IEA. *The Role of Critical Minerals in Clean Energy Transitions*. https://www.iea.org/reports/the-role-of-critical-minerals-in-clean-energy-transitions (2021).
2. Stinn, C. & Allanore, A. Selective sulfidation of metal compounds. *Nature* **602**, 78–83 (2022).
3. Su, C., Geng, Y., Zeng, X., Gao, Z. & Song, X. Uncovering the features of nickel flows in China. *Resour. Conserv. Recycl.* **188**, 106702 (2023).
4. U.S. Geological Survey. *Mineral Commodity Summaries 2023*. 210 http://pubs.er.usgs.gov/publication/mcs2023, https://doi.org/10.3133/mcs2023 (2023).
5. Hoatson, D. M., Jaireth, S. & Jaques, A. L. Nickel sulfide deposits in Australia: Characteristics, resources, and potential. *Ore Geol. Rev.* **29**, 177–241 (2006).
6. Xiao, W., Liu, X. & Zhao, Z. Kinetics of nickel leaching from low-nickel matte in sulfuric acid solution under atmospheric pressure. *Hydrometallurgy* **194**, 105353 (2020).
7. Schmidt, T., Buchert, M. & Schebek, L. Investigation of the primary production routes of nickel and cobalt products used for Li-ion batteries. *Resour. Conserv. Recycl.* **112**, 107–122 (2016).
8. Mudd, G. M. Global trends and environmental issues in nickel mining: Sulfides versus laterites. *Ore Geol. Rev.* **38**, 9–26 (2010).
9. Crundwell, F. K., Moats, M. S., Ramachandran, V., Robinson, T. G. & Davenport, W. G. Chapter 13 - Extraction of Nickel and Cobalt from Sulfide Ores. in *Extractive Metallurgy of Nickel, Cobalt and Platinum Group Metals* (eds. Crundwell, F. K., Moats, M. S., Ramachandran,

V., Robinson, T. G. & Davenport, W. G.) 147–158 (Elsevier, Oxford, 2011). https://doi.org/10.1016/B978-0-08-096809-4.10013-9.

10. Sun, Q. et al. Efficient Synchronous Extraction of Nickel, Copper, and Cobalt from Low–Nickel Matte by Sulfation Roasting–Water Leaching Process. *Sci. Rep.* **10**, 9916 (2020).

11. Warner, A. E. M. et al. JOM world nonferrous smelter survey Part IV: Nickel: Sulfide. *JOM* **59**, 58–72 (2007).

12. Faris, N., Pownceby, M. I., Bruckard, W. J. & Chen, M. The Direct Leaching of Nickel Sulfide Flotation Concentrates—A Historic and State-of-the-Art Review Part I: Piloted Processes and Commercial Operations. *Miner. Process. Extr. Metall. Rev.* **0**, 1–29 (2022).

13. Diaz, C. M., Landolt, C. A., Vahed, A., Warner, A. E. M. & Taylor, J. C. A Review of Nickel Pyrometallurgical Operations. *JOM* **40**, 28–33 (1988).

14. Winterhalder, K. Environmental degradation and rehabilitation of the landscape around Sudbury, a major mining and smelting area. *Environ. Rev.* **4**, 185–224 (1996).

15. Keller, W., Heneberry, J. & Edwards, B. A. Recovery of acidified Sudbury, Ontario, Canada, lakes: a multi-decade synthesis and update. *Environ. Rev.* **27**, 1–16 (2019).

16. Forward, F. A. & Mackiw, V. N. Chemistry of the Ammonia Pressure Process for Leaching Ni, Cu, and Co from Sherritt Gordon Sulphide Concentrates. *JOM* **7**, 457–463 (1955).

17. McDonald, R. G., Li, J. & Austin, P. J. High Temperature Pressure Oxidation of a Low-Grade Nickel Sulfide Concentrate with Control of the Residue Composition. *Minerals* **10**, 249 (2020).

18. Xie, K., Liu, S. & Wang, H. Oxidative Pressure Leaching of Nickel Sulfide Concentrate from Zambia. *Nonferrous Met. Extr. Metall.* **6**, 10 (2019).

19. Li, G. et al. A novel ammonium chloride roasting approach for the high-efficiency Co-sulfation of nickel, cobalt, and copper in polymetallic sulfide minerals. *Metall. Mater. Trans. B* **51**, 2769–2784 (2020).

20. Mu, W. et al. Extraction of copper and nickel from low-grade nickel sulfide ore by low-temperature roasting, selective decomposition and water-leaching process. *JOM* **71**, 4647–4658 (2019).

21. Watling, H. R. The bioleaching of nickel-copper sulfides. *Hydrometallurgy* **91**, 70–88 (2008).

22. Cruz, F. L., Oliveira, V. A., Guimarães, D., Souza, A. D. & Leão, V. A. High-temperature bioleaching of nickel sulfides: thermodynamic and kinetic implications. *Hydrometallurgy* **105**, 103–109 (2010).

23. Lotens, J. P. & Wesker, E. The behaviour of sulphur in the oxidative leaching of sulphidic minerals. *Hydrometallurgy* **18**, 39–54 (1987).

24. Lowson, R. T. Aqueous oxidation of pyrite by molecular oxygen. *Chem. Rev.* **82**, 461–497 (1982).

25. Tong, L. & Dreisinger, D. The adsorption of sulfur dispersing agents on sulfur and nickel sulfide concentrate surfaces. *Miner. Eng.* **22**, 445–450 (2009).

26. Kartal, M. et al. Enhancing chalcopyrite leaching by tetrachloroethylene-assisted removal of sulphur passivation and the mechanism of jarosite formation. *Hydrometallurgy* **191**, 105192 (2020).

27. Mackiw, V. N., Benz, T. W. & Evans, D. J. I. Recent developments in pressure hydrometallurgy. *Metall. Rev.* **11**, 143–158 (1966).

28. Lu, Z. Y., Jeffrey, M. I., Zhu, Y. & Lawson, F. Studies of pentlandite leaching in mixed oxygenated acidic chloride-sulfate solutions. *Hydrometallurgy* **56**, 63–74 (2000).

29. Subramanian, K. N. & Ferrajuolo, R. Oxygen pressure leaching of Fe-Ni-Cu sulfide concentrates at 110 °C — effect of low chloride addition. *Hydrometallurgy* **2**, 117–125 (1976).

30. Xu, C. et al. Extraction of metals from complex sulfide nickel concentrates by low-temperature chlorination roasting and water leaching. *Int. J. Miner. Metall. Mater.* **24**, 377–385 (2017).

31. Garg, S., Papangelakis, V., Edwards, E. & Mahadevan, R. Application of a selective dissolution protocol to quantify the terminal dissolution extents of pyrrhotite and pentlandite from pyrrhotite tailings. *Int. J. Miner. Process.* **158**, 27–34 (2017).

32. Kang, J., Yu, C., Liu, Z., Wang, Y. & Wang, X. Fe Migration and its Influence on the Oxidative Leaching of Low-Grade Ni–Cu–Fe-Bearing Sulfide Ores in Sulfuric Acid Solutions. *J. Sustain. Metall.* **9**, 723–737 (2023).

33. Faris, N., Pownceby, M. I., Bruckard, W. J. & Chen, M. The direct leaching of nickel sulfide flotation concentrates—a historic and state-of-the-art review part II: laboratory investigations into pressure leaching. *Miner. Process. Extr. Metall. Rev.* 1–23 https://doi.org/10.1080/08827508.2022.2084735 (2022).

34. Arpalahti, A. & Lundström, M. The leaching behavior of minerals from a pyrrhotite-rich pentlandite ore during heap leaching. *Miner. Eng.* **119**, 116–125 (2018).

35. Faris, N., Pownceby, M. I., Bruckard, W. J. & Chen, M. The direct leaching of nickel sulfide flotation concentrates—a historic and state-of-the-art review part III: laboratory investigations into atmospheric leach processes. *Miner. Process. Extr. Metall. Rev.* 1–21 https://doi.org/10.1080/08827508.2022.2098292 (2022).

36. Chapter 6 Chemical leaching of mechanically activated minerals. in *Process Metallurgy* (ed. BalÁž, P) vol. 10 143–193 (Elsevier, 2000).

37. Çetintaş, S., Yildiz, U. & Bingöl, D. A novel reagent-assisted mechanochemical method for nickel recovery from lateritic ore. *J. Clean. Prod.* **199**, 616–632 (2018).

38. Vafaeian, S., Ahmadian, M. & Rezaei, B. Sulphuric acid leaching of mechanically activated copper sulphidic concentrate. *Miner. Eng.* **24**, 1713–1716 (2011).

39. Lv, W. et al. A green recycling process for spent lithium-ion batteries with extremely low chemical consumption. *Fundam. Res.* https://doi.org/10.1016/j.fmre.2024.03.016 (2024).

40. Li, Z., Chen, M., Zhang, Q., Liu, X. & Saito, F. Mechanochemical processing of molybdenum and vanadium sulfides for metal recovery from spent catalysts wastes. *Waste Manag* **60**, 734–738 (2017).

41. Basturkcu, H., Achimovičová, M., Kaňuchová, M. & Acarkan, N. Mechanochemical pre-treatment of lateritic nickel ore with sulfur followed by atmospheric leaching. *Hydrometallurgy* **181**, 43–52 (2018).

42. Baláž, P., Aláčová, A., Achimovičová, M., Ficeriová, J. & Godočíková, E. Mechanochemistry in hydrometallurgy of sulphide minerals. *Hydrometallurgy* **77**, 9–17 (2005).

43. Yang, H. et al. Mechanical activation modes of chalcopyrite concentrate and relationship between microstructure and leaching efficiency. *Hydrometallurgy* **207**, 105778 (2022).

44. Zheng, X. et al. Leaching of valuable metals from nickel sulfide ores by mechanical activation. *Chin. J. Process Eng.* **21**, 1064 (2021).

45. Aram, R., Abdollahy, M., Pourghahramani, P., Darban, A. K. & Mohseni, M. Dissolution of mechanically activated sphalerite in the wet and dry milling conditions. *Powder Technol* **386**, 275–285 (2021).

46. Bhatti, T. M. & Yawar, W. Bacterial solubilization of phosphorus from phosphate rock containing sulfur-mud. *Hydrometallurgy* **103**, 54–59 (2010).

47. Baláž, P., Boldižárová, E., Achimovičová, M. & Kammel, R. Leaching and dissolution of a pentlandite concentrate pretreated by mechanical activation. *Hydrometallurgy* **57**, 85–96 (2000).

48. Janzen, M. P., Nicholson, R. V. & Scharer, J. M. Pyrrhotite reaction kinetics: reaction rates for oxidation by oxygen, ferric iron, and for nonoxidative dissolution. *Geochim. Cosmochim. Acta* **64**, 1511–1522 (2000).

49. Nesbitt, H. W., Bancroft, G. M., Pratt, A. R. & Scaini, M. J. Sulfur and iron surface states on fractured pyrite surfaces. *Am. Mineral.* **83**, 1067–1076 (1998).

50. Li, H. et al. In situ acid etching boosts mercury accommodation capacities of transition metal sulfides. *Nat. Commun.* **14**, 1395 (2023).

51. Wang, J. et al. Undercoordination chemistry of sulfur electro-catalyst in lithium–sulfur batteries. *Adv. Mater.* **36**, 2311019 (2024).

52. Hao, X. et al. Zn-vacancy mediated electron-hole separation in ZnS/g-C3N4 heterojunction for efficient visible-light photocatalytic hydrogen production. *Appl. Catal. B Environ.* **229**, 41–51 (2018).

53. Di, T., Zhu, B., Cheng, B., Yu, J. & Xu, J. A direct Z-scheme g-C3N4/SnS2 photocatalyst with superior visible-light CO2 reduction performance. *J. Catal.* **352**, 532–541 (2017).

54. Bafghi, M. S. H., Emami, A. H. & Zakeri, A. Effect of Specific Surface Area of a Mechanically Activated Chalcopyrite on Its Rate of Leaching in Sulfuric Acid-Ferric Sulfate Media. *Metall. Mater. Trans. B* **44**, 1166–1172 (2013).

55. Schmukat, A. et al. Leaching of metal(loid)s from a construction material: Influence of the particle size, specific surface area and ionic strength. *J. Hazard. Mater.* **227–228**, 257–264 (2012).

56. Xu, S., Zanin, M., Skinner, W. & Brito e Abreu, S. Surface chemistry of oxidised pyrite during grinding: ToF-SIMS and XPS surface analysis. *Miner. Eng.* **170**, 106992 (2021).

57. Nguyen, T. P. & Lefrant, S. XPS study of SiO thin films and SiO-metal interfaces. *J. Phys. Condens. Matter* **1**, 5197 (1989).

58. Nagaraj, D. R. & Brinen, J. S. SIMS and XPS study of the adsorption of sulfide collectors on pyroxene: a case for inadvert metal in activation. *Colloids Surf. Physicochem. Eng. Asp.* **116**, 241–249 (1996).

59. Liu, D., Zhang, G. & Li, B. Electrochemical and XPS investigations on the galvanic interaction between pentlandite and pyrrhotite in collectorless flotation system. *Miner. Eng.* **190**, 107916 (2022).

60. Legrand, D. L., Bancroft, G. M. & Nesbitt, H. W. Oxidation/alteration of pentlandite and pyrrhotite surfaces at pH 9.3: Part 1. Assignment of XPS spectra and chemical trends. *Am. Mineral.* **90**, 1042–1054 (2005).

61. Payne, B. P., Biesinger, M. C. & McIntyre, N. S. Use of oxygen/nickel ratios in the XPS characterisation of oxide phases on nickel metal and nickel alloy surfaces. *J. Electron Spectrosc. Relat. Phenom.* **185**, 159–166 (2012).

62. Payne, B. P., Biesinger, M. C. & McIntyre, N. S. The study of polycrystalline nickel metal oxidation by water vapour. *J. Electron Spectrosc. Relat. Phenom.* **175**, 55–65 (2009).

63. Hu, H., Chen, Q., Yin, Z., Zhang, P. & Wang, G. Effect of grinding atmosphere on the leaching of mechanically activated pyrite and sphalerite. *Hydrometallurgy* **72**, 79–86 (2004).

64. Thomas, J. E., Jones, C. F., Skinner, W. M. & Smart, R. The role of surface sulfur species in the inhibition of pyrrhotite dissolution in acid conditions. *Geochim. Cosmochim. Acta* **62**, 1555–1565 (1998).

65. Zhou, W. et al. Ni3S2 nanorods/Ni foam composite electrode with low overpotential for electrocatalytic oxygen evolution. *Energy Environ. Sci.* **6**, 2921–2924 (2013).

66. Mkhonto, P. P., Chauke, H. R. & Ngoepe, P. E. Ab initio Studies of O2 Adsorption on (110) Nickel-Rich Pentlandite (Fe4Ni5S8) Mineral Surface. *Minerals* **5**, 665–678 (2015).

67. Xiong, X. et al. Oxidation mechanism of chalcopyrite revealed by X-ray photoelectron spectroscopy and first principles studies. *Appl. Surf. Sci.* **427**, 233–241 (2018).

68. Liu, X. et al. Nickel leaching kinetics of high-grade nickel matte with sulfuric acid under atmospheric pressure. *Hydrometallurgy* **215**, 105987 (2023).

69. Wang, Y., Lyu, Y., Wang, S. & Du, H. Generation of reactive oxygen species from oxygen microbubbles in phosphoric acid solution and its application of ferrous iron oxidation. *J. Taiwan Inst. Chem. Eng.* **125**, 195–203 (2021).

70. Takahashi, M., Chiba, K. & Li, P. Free-Radical Generation from Collapsing Microbubbles in the Absence of a Dynamic Stimulus. *J. Phys. Chem. B* **111**, 1343–1347 (2007).

71. Wood, P. M. The potential diagram for oxygen at pH 7. *Biochem. J.* **253**, 287–289 (1988).

Acknowledgements

Author contributions

Q.Z., X.Z., and Z.S. conceived the idea and designed the experiments. Q.Z., W.L., and M.H. contributed to the characterization. Q.Z., W.Y., W.G., and P.N. carried out the data analysis. Q.Z., H.C., and Z.S. wrote the manuscript. All authors contribute to the discussion and revision of the final manuscript.

Competing interests

The authors declare no competing interests.

Additional information

Supplementary information The online version contains supplementary material available at https://doi.org/10.1038/s41467-025-59995-6.

Correspondence and requests for materials should be addressed to Hongbin Cao or Zhi Sun.

Peer review information *Nature Communications* thanks Hüseyin Baştürkcü, Zhenming Xu and the other, anonymous, reviewer(s) for their contribution to the peer review of this work. A peer review file is available.

Reprints and permissions information is available at http://www.nature.com/reprints

Publisher's note Springer Nature remains neutral with regard to jurisdictional claims in published maps and institutional affiliations.